DOI: 10.15480/882.9312

Eighth International Symposium on Marine Propulsors
smp'24, Berlin, Germany, March 2024

Direct Numerical Simulation of the Centrifugal Instability-induced Transition Around a Marine Propeller Blade.

Bastien Boudenne[1], **Antoine Ducoin**[1]

[1]Nantes Université, École Centrale Nantes, CNRS, LHEEA, UMR 6598, F-44000 Nantes, France

ABSTRACT

The boundary layer regime knowledge is a key factor in predicting the performance of lab-scale marine propellers. Even if the distribution of the boundary layer flow regime around the propeller blade is well-known by the marine propeller community, no dynamic of the turbulent process has already been reported in the literature. An Under-resolved Direct Numerical Simulation (U-DNS) of a C-series marine propeller blade at a Reynolds number of $600,000$ and an advance coefficient of 0.73 is performed to gain insights into the turbulent transition mechanisms of the boundary layer. An overset approach is used with the open-source spectral element code Nek5000 to optimize the computational cost of the simulation. After performing a mesh-sensitivity analysis, results are validated using experimental data. The detailed investigation of the boundary layer shows good agreement with the experimental and numerical data. New insights into the turbulent transition dynamics suggest that centrifugal instability plays a major role in the transition process. A map of the boundary layer flow regimes is then discussed. The laminar cross-flow vortices' inception and breakdown are studied in detail to characterize the onset of longitudinal streaks.

Keywords

Turbulent Transition, Marine Propeller, DNS, CFD

1 INTRODUCTION

Boundary layer transition in naval propulsion applications holds significant importance as it directly impacts the efficiency and performance of ships. Full-scale propellers operate at a high Reynolds number (10^9), and their boundary layer is generally considered fully turbulent. However, a transitional boundary layer tends to develop on smaller or model scale propellers as the Reynolds number decreases to values below 10^6. Boundary layer regimes significantly impact drag reduction and thrust enhancement. Efficiently managing the turbulent transition is essential, as it optimizes marine propeller blade design. Early studies from the late 1970s investigated the correlation between cavitation inception and the boundary layer regimes. It allowed researchers (Kuiper 1978; Jessup et al. 2018) to draw flow maps predominantly focused on the suction side of the propeller blade due to the complex flow regime distribution observed during testing.

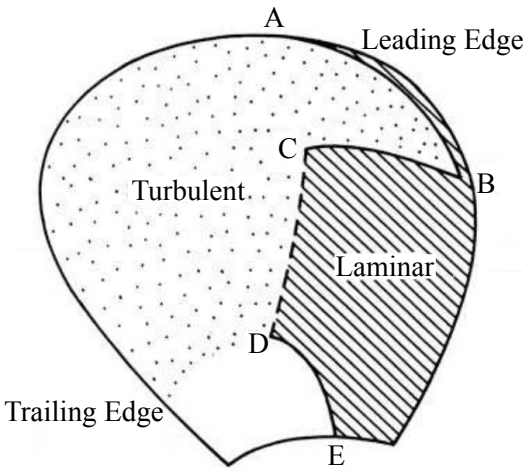

Figure 1: Scheme of the flow regime over the suction side of a propeller blade, from (Carlton 1978). AB - Laminar Separation Bubble (LSB). BC - Critical Radius. CD - Transition. DE - Separation.

Figure **??** extracted from (Carlton 2018) provides an overview of the flow features encountered at the suction side. Near the leading edge along the AB segment, a Laminar Bubble Separation (LBS)-induced transition occurs in the boundary layer due to a destabilizing (adverse) pressure gradient leading to a fully turbulent boundary layer flow downstream. The BC segment bounding the LSB-induced transition region at the leading edge is commonly designated as critical radius, denoted R_{crit}. Kuiper (1978) observed that this critical radius changes with the propeller blade's loading but remains independent of the Reynolds number. Below the critical radius, the CD segment corresponds to a turbulent transition of the boundary layer flow. However, the literature does not report any specific transition mechanism. Closer to the blade's root, downstream of the DE line, the flow remains laminar and separated due to the relatively low velocity. He also notes that the transition occurs along the entire span of the blade on the pressure side. The absence of destabilizing (adverse) pressure gradient on the pressure side simplifies the flow map, although specific transition mechanisms are not specified. Carlton (2018) confirms that no LSB is observed on the pressure side and notes a significant laminar boundary layer on the pressure side.

Historically, flow maps were obtained using painted propellers

to observe the boundary layer flow regime on propeller surfaces. Various studies used this method (Kuiper 1978) (Jessup et al. 1985) or relied on interferometry techniques (Shüelein et al. 2012) to extract friction lines from the propeller surface.

With the paint coating technique, the flow self-spreads the painting across the blade surface, leaving friction line patterns. From the tested propeller blades, the C-series propeller blades exhibited deviated friction lines on both sides of the blade. The orientation of the skin friction lines undergoes a transition from laminar flow (spanwise direction) to turbulent flow (chordwise), highlighting the transition region (Schüelein et al 2012).

Measurements of the boundary layer quantities are challenging on rotating blades, and limited experimental data are available in the literature. Consequently, Computational Fluid Dynamics (CFD) is often used to conduct a finer analysis. To the author's knowledge, CFD simulations that have explored boundary layer flow around marine propellers have relied on Reynolds Averaged Navier-Stokes (RANS) simulations. The turbulent transition is modeled with a transition model relying on empirical correlations, as the $\gamma - Re_\theta$ model. This transition model has two transport equations capable of accurately predicting the overall boundary layer regimes.

Baltazar et al. (2018) conducted RANS simulations coupled with the $\gamma - Re_\theta$ transition model on several propeller blades. Their study revealed that the transition model slightly improved the skin friction pattern and increased the thrust prediction, as it left room for the laminar boundary layer to develop. The authors observed a high sensitivity of the results when modifying the inlet turbulence parameters. Pawar & Brizzolara (2019a) also observed a strong dependence between the transition location and the turbulent viscosity ratio set at the inlet when simulating the flow over a C-series marine propeller. Comparison of the results with the painting experiments showed the presence of a transitional boundary layer on the pressure side using the $\gamma - Re_\theta$ model. While this approach captures the overall boundary layer regime, it fails to describe the dynamics of the transition process.

One of the limitations of such methods is the necessity to calibrate simulation results by comparing them to painted-propeller experiments, as outlined in (Baltazar et al. 2019). In the context of marine propellers, the high-speed rotating motion induces significant centrifugal force, leading to the development of a cross-flow into the boundary layer. Reed & Saric (2003) presented different types of turbulent transition mechanisms. Amongst them, the study of the boundary layer flow over a rotating disc showed that centrifugal force controls the transition process. A detailed description of its dynamic is available in (Kohama 1984). A long coherent longitudinal vortex (streak) emerges as the cross-flow develops in the boundary layer. The number of longitudinal vortices observed experimentally varies (Wilkinson & Malik 1985). However, all agree that the inception of a secondary instability creates ring-like vortices around the streak (centrifugal instability), destabilizing it until reaching the turbulent regime.

More recently, new simulations shed light on the possible existence of cross-flow at the blade's surface. Pawar & Brizzolara (2019b) performed RANS simulations using the $k-\omega$ SST turbulence model coupled with the $\gamma - Re_\theta$ transition model. The close wall mesh resolution is characterized by a y^+_{wall} ranging between 1 and 2 in the turbulent regions. To validate the numerical setup, Pawar & Brizzolara simulate the flow around a B-series Wageningen propeller blade before investigating the turbulent transition around a ducted marine propeller. At a low advance coefficient (J=0.1), their simulation shows streaks of high friction close to the trailing edge at the pressure side in the presence of high centrifugal forces.

Moran-Guerrerro et al. (2018) introduced an additional cross-flow term in the $\gamma - Re_\theta$ model to add the influence of cross-flow in the transition process. The results indicated that this new term increased the skin friction coefficients on the suction side. The local helicity of the fluid showed the occurrence of cross-flow vortices developing on the suction side as a result of these changes.

Jing & Ducoin (2020) conducted an Under-resolved Direct Numerical Simulation (U-DNS) of the boundary layer flow around a C-series marine propeller blade. Their study also pointed out cross-flow vortices and centrifugal instabilities developing on the suction side, extending from the blade tip up to a critical radius located around 85% of the blade radius. Laminar cross-flow began to develop near the trailing edge on the pressure side. However, the Reynolds number $(220,000)$ used in their simulation was too low to complete the turbulent transition. This Reynolds number corresponds to only a third of the experimental conditions documented in (Kuiper 1978). Therefore, the study's findings are limited as no corresponding operating conditions are available in the literature.

This study uses the same C-series marine propeller blade as Kuiper (1978) and Jing & Ducoin (2020). The Reynolds number is increased to $600,000$ to match Kuiper's operating condition. The main objective of this paper is to present a U-DNS of the transitional boundary layer flow on a lab-scale marine propeller blade and to demonstrate the significant role played by centrifugal effects in the transition process, particularly on the blade's pressure side.

2 METHOD

2.1 Numerical Domain

The present study relies on a four-blade C-series marine propeller. The blade's low aspect ratio increases the likelihood of experiencing transition induced by centrifugal instability. Kuiper (1978) investigated the boundary layer regime in the towing tank without cavitation, making it possible to perform the present numerical simulation under monophasic and incompressible conditions.

The C-series marine propeller blade described in (Kuiper 1978) sees a uniform flow in open-water conditions with a flow velocity $U_z = 5.45\ m.s^{-1}$ to investigate the laminar-to-turbulent transition around the blade. The propeller scale is conserved with a blade radius of $R_b = 0.15\ m$ and a hub of $R_{hub} = 0.31R_b$ to match the experiment conditions.

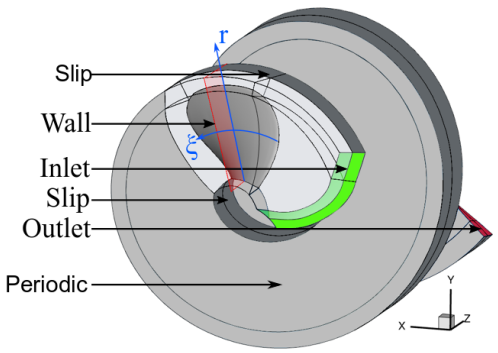

Figure 2: Near-wall domain capturing the boundary layer flow. The domain shown above corresponds to the close wall mesh.

The rotational rate is set to $n = 7.92\ rev.s^{-1}$ to keep the Reynolds number of the propeller blade at $Re_n = 4\rho n R_b^2/\mu = 600,000$ where $\rho = 1025.9\ kg.m^{-3}$ the salt-water density, and $\mu = 1.22 \times 10^{-3}\ Pa.s$ its dynamic viscosity at 3.5% salinity. The advance coefficient of $J = U_z/(2\pi n R_b) = 0.73$ sets the advancing velocity value U_z.

Available computational resources allowed us to model only one blade. Additionally, the simulation is performed in the fixed blade's reference frame. The Navier-Stokes equations are completed with the Coriolis acceleration and the centrifugal forcing terms to simulate the rotating motion of the system.

As illustrated in Figure **??**, the domain's helicoidal shape is designed to capture accurately the propeller blade's wake. At the hub boundary, a free-slip condition is imposed to present the development of spurious boundary layer interaction with the one from the blade.

The choice of reference frame induces a laminar non-uniform velocity profile at the inlet of the domain, $1.8R_b$ upstream. The coarse mesh in the far field prevents synthetic turbulence from significantly affecting the boundary layer, as it would effectively filter it out. No local volumic forces are applied to the wall region to mimic the degraded wall surface obtained experimentally with the painting (Kuiper 1978). The numerical domain extends $3.2R_b$ downstream from the propeller with a zero-pressure gradient outflow condition. The domain's frontiers on each blade's side have periodic boundary conditions. It allows us to model the flow around a four-blade propeller using circumferential periodicity, effectively capturing the possible wake interactions among the blades in the far downstream field. However, due to the mesh coarsening as we move away from the propeller blade surface, the DNS mesh only focuses on the near-wall region and only captures the larger wake interaction.

2.2 Mesh Definition

The objective of the present simulation is to capture the boundary layer flow at the blade surface. An overset approach has been used to mesh the computational domain to keep a high spatial resolution near the blade while optimizing the number of computational nodes.

Jing & Ducoin (2020) have already described the mesh used in this study. This method uses two fixed overlapping meshes. Cutting a slice of the domain, colored in red in Figure-**??**, allows us to see the structure of each mesh. The close-wall mesh colored in red in Figure **??**, spreads from the propeller blade's surface following the surface normal and gets finer in the boundary layer region with at least ten spectral elements to accurately capture the flow dynamics close to the wall. The close wall mesh has 943 200 elements in total, ranging from $r = R_{hub}$ to $r = 1.1R_b$.

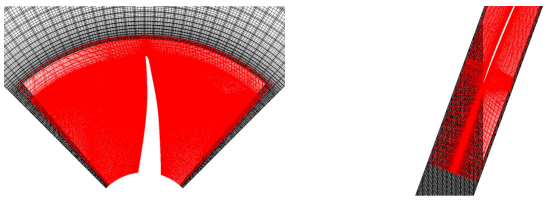

(a) (r,ξ)-plane **(b) (ξ,η)-plane**

Figure 3: Slices of the overlapping mesh used for the present simulation. From (Jing & Ducoin 2020). The close-wall mesh is colored red, and the background mesh is gray.

The background mesh, shown in gray in Figure-**??**, is coarser and is composed of 216 875 elements. It solves the flow far from the blade's surface for $1.1R_b \leq r < 3R_b$. In this region, the flow can be considered undisturbed by the propeller motion and is assumed inviscid and steady. The discretization of the entire fluid domain has 1 160 075 spectral elements.

2.3 Coordinate System

The simulation is performed in the propeller reference frame to save computational time. The domain has a helicoidal shape to take the rotation of the blade around the z-axis into account (see Figure **??**). The z-axis points towards the propeller blade's wake, and the y-axis coincides with the directrix. The x-axis' orientation completes the coordinate system to have a direct basis. The origin of the reference frame overlaps the center of the hub, out of the scope of the present study.

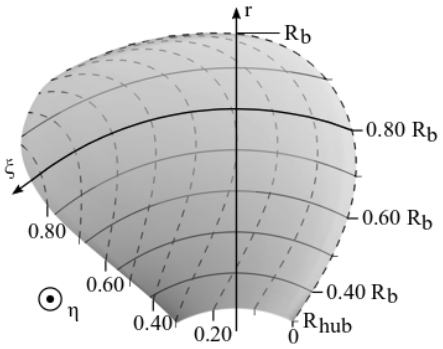

Figure 4: Definition of the local coordinate system of the propeller blade.

A new set of coordinates is defined to have relevant variables for the fluid flow investigation. Figure **??** shows the variables used in the rest of the study, with ξ the chordwise position from the leading edge at a constant radius, r the radial position, and η the distance from the blade surface. The leading edge is defined as $\xi = \eta = 0$ and the trailing edge as $\xi = c(r), \eta = 0$, where $c(r)$ is the local blade chord at radius r.

2.4 Nek5000 Code

The simulation solves the Navier-Stokes equations in a rotating reference frame using the Nek5000 CFD code developed by the Argonne Lab (Nek5000 2019). This solver is based on the Spectral Element Method (SEM) using high-order Galerkin's projection methods (Fischer et al. 2008).

The simulation is performed using the 6^{th}, 8^{th}, and 10^{th} spectral orders for the same mesh design to ensure the mesh independence of the results. The simulation is then launched using the P_n-P_{n-2} formulation described in (Maday & Patera 1989).

Nek5000 is highly scalable and allows us to perform DNS simulations on the supercomputer Jean-Zay HPE SGI8600 (CPU partition) at the national cluster GENCI-IDRIS, Paris, France.

2.5 Initial Condition and Solution Convergence

During the initialization, the inlet flow velocity is imposed throughout the domain. The simulation convergence is performed in two steps. First, the simulation is launched with a deprecated mesh resolution (spectral order of 4) and an inviscid flow to converge the background mesh. Then, the spectral order is increased in the entire domain to converge the inner mesh with a viscous flow.

Three spectral order elements are used to investigate the sensitiv-

ity of the mesh. First, the simulation is realized using the 6^{th} and 8^{th} spectral order elements (O(6) and O(8)). The meshes count $250,576,200$ (O(6)) and $593,958,400$ (O(8)) nodes. The simulation lasted respectively $160,000$ (O(6)) and 1.8 million (O(8)) CPUh on 8912 processors.

For both meshes, the simulation extends up to $0.12\ s$ of physical time after the numerical convergence of the solution. It allows us to obtain the mean flow and also perform spectral analysis. Finally, simulation at order 10 (O(10)) is carried out from the solution at order 8. Due to limited computational resources, only numerical convergence is obtained. The limited physical time available prevents gathering sufficient statistics for mean flow calculation. It would require 5 million CPU hours to obtain $0.12\ s$ of physical time to compare with O(6) and O(8) meshes, which were considered too significant for a single calculation. Hence, the simulation at O(10) is only used in the sensitivity analysis.

3 RESULTS

Using the method described above, the simulation of a C-series propeller in open-water conditions with an advancing coefficient $J = 0.73$ gives the following results. The open-water characteristic coefficients presented are the thrust coefficient K_T and the torque coefficient K_Q defined as : $K_T = T/\left(16\rho n^2 R_b^4\right)$ and $K_Q = Q/\left(32\rho n^2 R_b^5\right)$, where T is the propeller thrust, Q the propeller torque.

The skin friction coefficient C_f is used to analyze the local performances of the propeller blade. The same definition as in (Pawar & Brizzolara 2019a) is employed, with $SKF = C_f = \tau_w/\left(\rho U_{in}^2(r)\right)$. Where τ_w is the local wall shear stress magnitude, and $U_{in}(r) = \sqrt{U_z^2 + (\omega r)^2}$ is the local incident velocity.

3.1 Convergence of the Simulation

One of the critical criteria for assessing the validity of a solution in boundary layer analysis is to evaluate the close-wall resolution. The three different meshes are compared to this end.

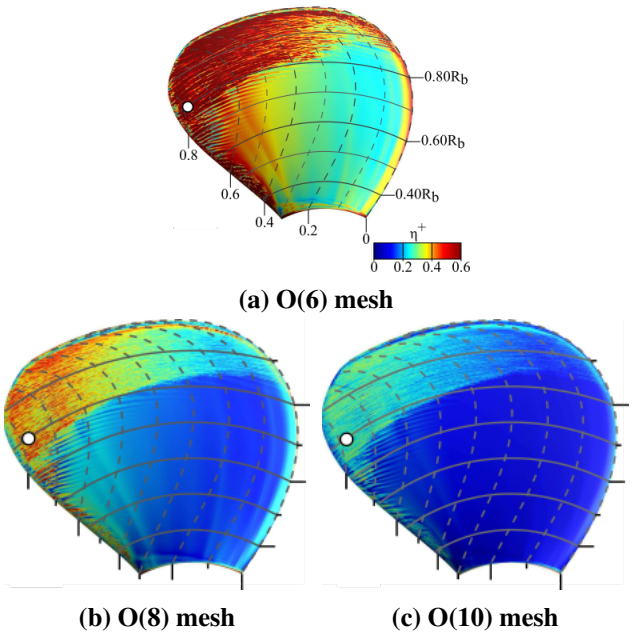

(a) O(6) mesh

(b) O(8) mesh (c) O(10) mesh

Figure 5: Mean η^+ values obtained at the propeller suction side using the 6, 8, and 10 spectral order meshes. The flow is averaged over 0.0267 s. White dots correspond to the velocity profile location plotted in Figure ??.

Figure **??** illustrates the distribution of the dimensionless distance η^+ of the first computational node to the wall at the suction side of the blade. According to Kuiper (1978) and Jing & Ducoin (2020), the flow is turbulent at a radius of $r = 0.85R_b$. The average η^+ values in the turbulent wall region are approximately 0.3 and 0.4 for O(8) and O(10), respectively, and around 0.6 or higher for the O(6) mesh. According to Choi & Moin (2012), the latter values are too large for achieving a full DNS over the blade surface. However, the η^+ values at O(8) and O(10) are sufficiently low for accurately capturing the transitional flow.

Given that the η^+ value is slightly too high to perform a fully resolved Direct Numerical Simulation (DNS) in the turbulent wall region, an Under-resolved DNS (U-DNS) is carried out. Hence, the capture of the fully turbulent boundary layer is out of the scope of the present work to set the focus on transitional flow prediction.

The velocity profiles in the turbulent region for the three different mesh orders are presented in Figure **??**. The profiles are averaged over $t_{avg} = 0.027\ s$, corresponding to the maximum physical time obtained at O(10). The fully averaged ($t_{avg} = 0.12\ s$) boundary layer at O(8) is plotted for reference. Figure **??** shows that the turbulent velocity profile at O(6) fails to accurately predict the linear sublayer of the turbulent boundary layer, resulting in an underestimation of the friction velocity. In contrast, the profiles at O(8) and O(10) are similar.

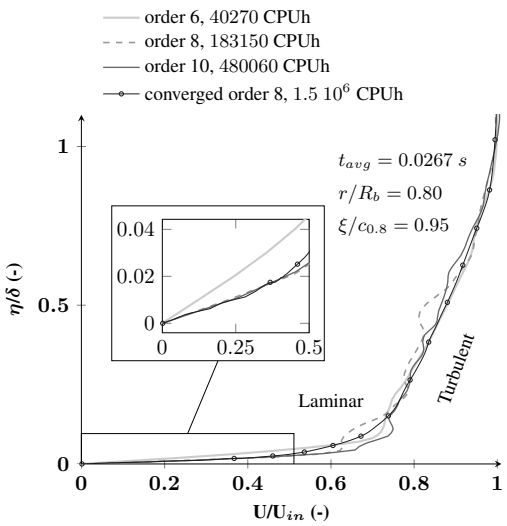

Figure 6: Comparison of the different turbulent velocity profiles for the 6, 8, and 10 spectral element meshes. The velocity profiles are taken at the same point, in the turbulent region at the suction side. Each velocity profile is given using data averaged over $0.0267\ s$.

The spatial resolution of the O(6) mesh is insufficient for accurately predicting the boundary layer flow. The O(8) and O(10) meshes yield more accurate and nearly identical results, even for the turbulent boundary layer. Therefore, the O(8) mesh is selected to investigate the transitional boundary layer on the blade.

3.2 Open-water Characteristics

Numerical simulations of global forces are compared with experimental data from Kuiper (1978) at an advance ratio of $J = 0.73$, and the results for thrust and torque coefficients are presented in Table **??**.

The present numerical data are averaged over a time window of $0.12\ s$ and exhibit good agreement with the experimental results

obtained by Kuiper (1978) and Jing & Ducoin (2020). As expected, previous simulation conducted at a lower Reynolds number of $Re_n = 220,000$ predicted significantly higher values for both thrust coefficient (K_T) and torque coefficient (K_Q), reflecting the predominantly laminar flow over the entire blade in this case.

3.3 Analysis of the Boundary Layer Regime

Kuiper (1978) employed coated blades to determine the orientation of the friction lines on both sides of the propeller blades. The deviation of these lines indicates a transition in the boundary layer flow regime, as depicted in Figure **??**(a). Depending on the orientation of the friction lines, it is commonly accepted to observe either laminar flow (spanwise direction) or turbulent flow (chordwise). The same behavior is observed numerically in the RANS simulation of Pawar & Brizzolara (2019a), the U-DNS simulations of Jing & Ducoin (2020), and the present simulation.

Table 1: Comparison of the thrust coefficient K_T and the torque coefficient K_Q between experimental data and previous DNS simulation, at $J = 0.73$.

	K_T	Error K_T
Exp MARIN (Kuiper 1978)	0.3466	-
DNS, O(8) ($Re_n = 2.2\ 10^5$) (Jing & Ducoin 2020)	0.388	12.0%
DNS, O(8) ($Re_n = 6.0\ 10^5$)	0.353	1.71%
	$10K_Q$	Error $10K_Q$
Exp MARIN (Kuiper 1978)	0.1921	-
DNS, O(8) ($Re_n = 2.2\ 10^5$) (Jing & Ducoin 2020)	0.220	14.5%
DNS, O(8) ($Re_n = 6.0\ 10^5$)	0.200	4.0%

In Figure **??**(c), the friction line deflection is sharper than in the RANS simulation (see Figure **??**(b)). From the orientation of the friction lines on the suction side, one can distinguish two distinct regions: one with a low skin friction coefficient C_f where the friction lines point towards the blade tip, suggesting that centrifugal force controls the boundary layer flow regime in this region. The second region, located in the sudden rises of the C_f, shows friction lines sharply turning towards the trailing edge, indicating that inertia plays a significant role in the transition between the flow regimes. This sudden change in direction triggers a rapid transition from laminar to turbulent flow.

The critical radius, denoted as R_{crit}, which indicates the point where the boundary layer transitions to turbulence at the leading edge, has been well-documented by Kuiper (1978) to be approximately at $r = 0.85R_b$. The simulation of Pawar & Brizzolara (2019a) also detects a critical radius in Figure **??**(b) but misses to locate it correctly and finds it around $r = 0.9R_b$. In the recent U-DNS study, this critical radius is between $0.85R_b$ (Jing & Ducoin 2020) and $0.84R_b$ in the current simulation. This consistency, along with the quasi-independence between the Reynolds number and the critical radius value, as also noted in Kuiper (1978), reinforces the findings of the present simulation. For inner radii, specifically within the range of $0.6R_b \leq r \leq 0.84R_b$, Figure **??**(c) shows the progressive transition of the boundary layer flow toward turbulence from $\xi = 0.6$ extending up to the trailing edge for $0.7R_b \leq r \leq 0.8R_b$. The rise of the skin friction coefficient is faster in the present DNS that reaches $C_f = 0.005$ and remains constant on the turbulent region, while Figure **??**(b) shows a more progressive increase in the skin friction to reach 0.00425 downstream of the laminar-to-turbulent transition.

On the pressure side, the deviation of the friction line in the chordwise direction throughout the blade's span is consistently observed, except near the blade's tip, where the blade tip's influence may come into play. Downstream for the fiction line deviation the skin friction is higher than in the RANS simulation. Figure **??**(c) illustrates the presence of streaks of high friction, as in (Pawar & Brizzolara 2019b) at lower J.

The change in the orientation of the friction line appears to coincide with the inception of the laminar longitudinal streaks rather than when the transition onset to turbulence.

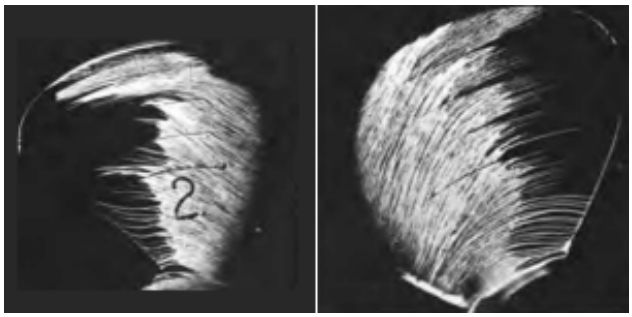

(a) Exp.(Kuiper 1978)

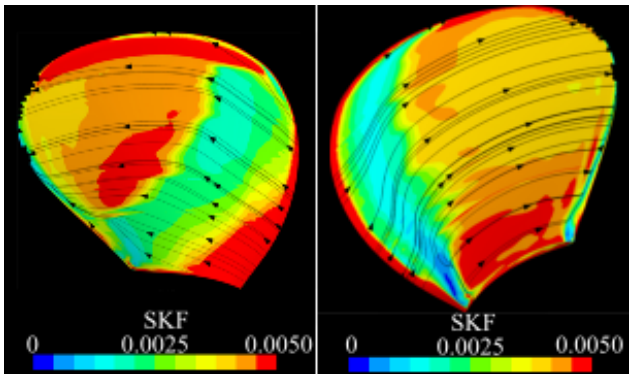

(b) RANS + $\gamma - Re_\theta$ (modified from (Pawar & Brizzolara 2019a))

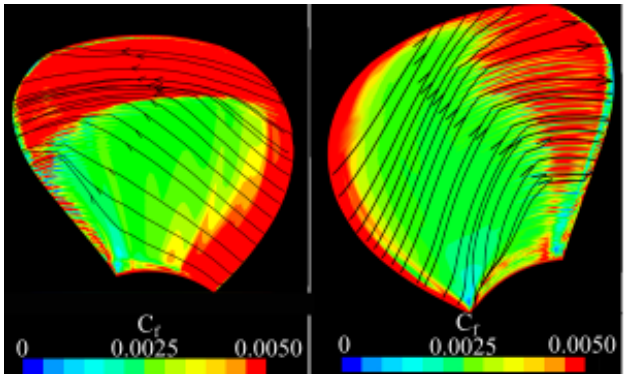

(c) Pres. DNS

Figure 7: Comparison of the friction line at the blade'surfacese. Numerical results also show the skin friction coefficient. Left: Suction side, Right: Pressure side

On both sides of the blade, the overall flow topology matches the experimental results shown in Figure **??**(a) and the numerical results in Figure **??**(b), although the friction line deviation is slightly delayed in the current simulation. This discrepancy might be attributed to differences in surface roughness between the ex-

periments and the numerical domain, as well as the difference in turbulence intensity between the towing tank (3% of turbulent intensity (Kuiper 1978)) and the present U-DNS (purely laminar flow).

The coherent structures displayed in Figure **??** and Figure **??** also provide insight into the various boundary layer regimes surrounding the propeller blade. On the suction side, Figure **??**(a) shows that laminar cross-flow vortices are maintained up to the trailing edge, except near the blade tip where a turbulent region is observed. As the Reynolds number increases, the current simulation in Figure **??**(a) shows a sharp transition at the leading edge from the critical radius $R_{crit} = 0.84R_b$ up to the blade's tip.

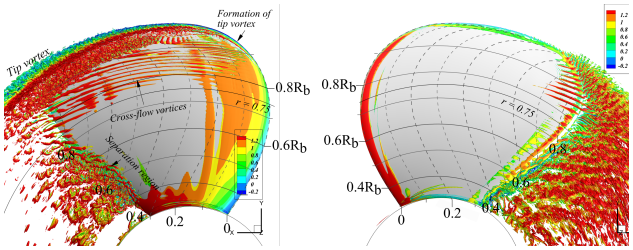

(a) Suction side **(b) Pressure side**

Figure 8: Instantaneous coherent structures detected with λ_2-criterion set to -1250, at $Re_n = 200,000$, modified from (Jing & Ducoin 2020). Isosurfaces are colored according to the absolute velocity magnitude.

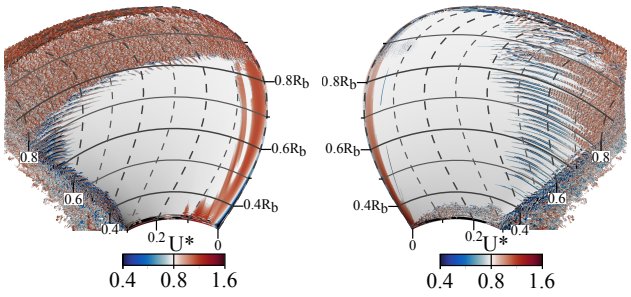

(a) Suction side **(b) Pressure side**

Figure 9: Instantaneous coherent structures detected with λ_2-criterion set to -2500. Iso-surfaces are colored according to the normalized velocity magnitude $U^* = U_{mag}/U_{in}$.

Below the critical radius, longitudinal vortices develop due to centrifugal forces. These streaks begin to develop from $\xi = 0.6$, but the boundary layer remains predominantly laminar until it reaches the trailing edge. Figure **??**(a) and Figure **??**(b) complete the description of the boundary layer regimes offered by Figure **??**(c). The friction lines deviate as the friction coefficient increases. Longitudinal streaks develop beneath the fully turbulent region, bounded by the critical radius on the suction side from $r = 0.6R_b$ to $0.8R_b$. Close to the trailing edge ($\xi \geq 0.7$), ring-like vortices emerge before the inception of turbulent structures for r between $0.65R_b$ and $0.75R_b$.

Figure **??**(b) shows that for the lower Reynolds number case, longitudinal streaks begin to develop at the trailing edge from $r = 0.80R_b$ up to the blade's tip close to the trailing edge ($\xi \geq 0.7$). The increase in Reynolds number causes the longitudinal streaks to propagate across a significant part of the pressure side before undergoing a turbulent transition through centrifugal instabilities (see Figure **??**(b)). These streaks are present on the entire blade's span, although their inception seems influenced by the blade's tip vortex for $r > 0.9R_b$. The inception of the centrifugal instabilities in Figure **??** shows to occur downstream from the friction line deflection in Figure **??**(c). Hence, the friction line behavior seems to be highly influenced by the occurrence of the longitudinal streaks (see Figure **??**(b)). Figure **??**(b) illustrates the streaks breakdown as centrifugal-instabilities structures emerge close to the trailing edge before becoming fully turbulent, which could not be seen in Figure **??**, where the flow is time-averaged.

From the experimental painted results (see Figure **??**(a)), one expects to observe an increase in the skin friction coefficient in regions where the paint patterns exhibit changes in direction. This behavior is also present in Figure **??**(c), where it becomes evident that the skin friction increases as longitudinal streaks emerge. The long longitudinal streaks develop on the pressure side, extending from $\xi = 0.3$ to the trailing edge. These streaks correlate with a rise in the friction coefficient and with the deflection of the friction line across the entire span of the propeller blade, as depicted in Figure **??**(c). As interpreted from Figure **??**(b), the skin friction coefficient rises when encountering longitudinal streaks, even in laminar regions.

3.4 Investigation of the Transitional Boundary Layer Flow

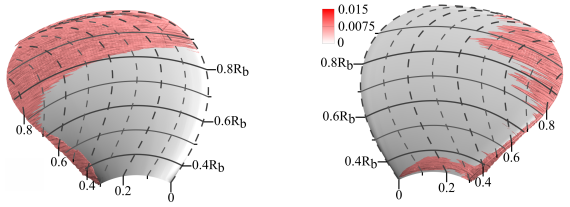

(a) Suction side **(b) Pressure side**

Figure 10: Dimensionless turbulent kinetic energy $2k'/(\rho U_{in}^2)$ appearance over the propeller blade. The isosurface is set to 0.0075 using the averaged flow.

The distribution of turbulent kinetic energy (TKE) around the propeller blade is investigated in Figure **??** to validate the correlation between streak inception and friction line deflection. Figure **??** depicts the isosurface for 0.75% of the freestream's kinetic energy as the onset of the turbulence creation. Figure **??**(a) shows a strong correlation between the deviation of the friction line, the increase in skin friction, and the turbulent transition of the boundary layer flow on the suction side. However, on the pressure side, a different dynamic takes place. Significant discrepancies emerge between the deflection location of the friction line and the onset of TKE for radii up to $0.84R_b$, as shown in Figure **??**(b). In the range of $0.7R_b \leq r \leq 0.82R_b$, the flow undergoes transition around $\xi = 0.6$, deviating from the expected $\xi = 0.3$ suggested by the analysis of the friction line (Kuiper 1978). For inner radii, a similar pattern is shown in Figure **??**(c), with friction line deflection occurring between $\xi = 0.4$ and $\xi = 0.5$, while a turbulent transition is observed at the trailing edge, as depicted in Figure **??**(b). Based on the analysis of the boundary layer flow in this study, one can create an updated map of the boundary layer flow regimes for both sides of the blade. Figure **??** overlaps the coherent structures observed at the blade surface with the boundary layer regimes.

On both sides of the blade, the laminar regions extend from the inception of streaks (indicated by dotted-red lines) up to the onset

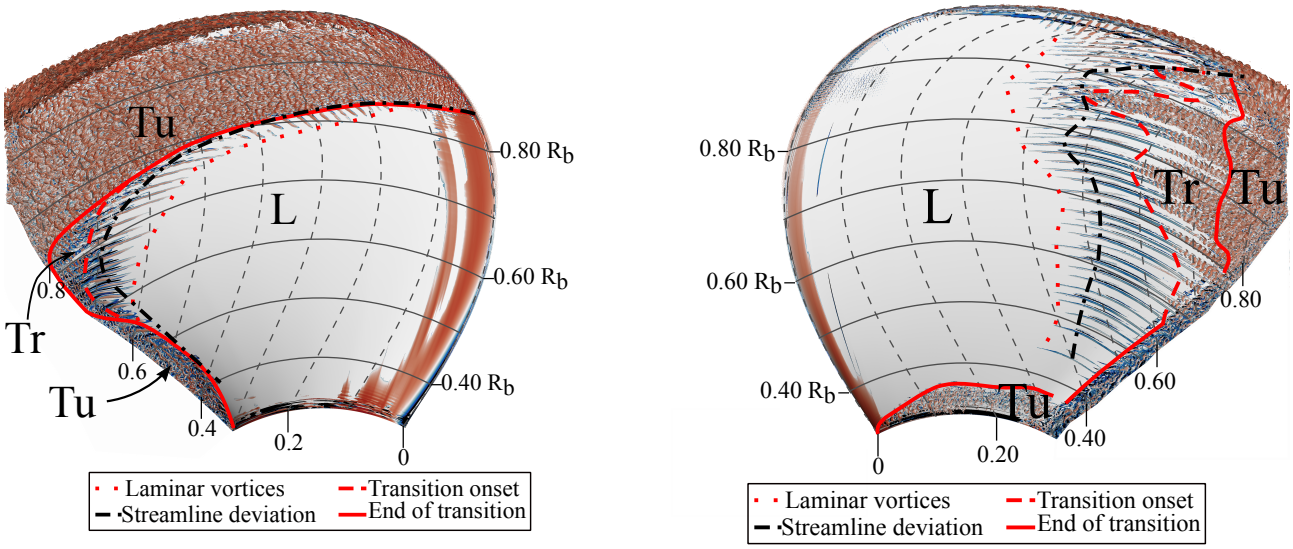

(a) Suction side **(b) Pressure side**

Figure 11: Flow regime observed on the front and back of the C-series marine propeller blade. Instantaneous coherent structures are colored using relative velocity magnitude $U_{mag}/U_{in}(r)$. Shaded dashed lines correspond to the r and ξ-iso values.

of transition (marked by the continuous-red lines). The sudden rise of TKE at the blade's surface gives insights into the transition onset. Notably, the transition region covers a larger area on the pressure side (see Figure **??**(b)) compared to the suction side (see Figure **??**(a)), where it is localized near the trailing edge, spanning from $r = 0.5R_b$ to $0.8R_b$.

One can compare the flow map at the suction side with Figure **??**(a) extracted from (Carlton 2018). Both reveal a large turbulent region extending to the critical radius at $R_{crit} = 0.84R_b$. However, the present U-DNS does not detect an LSB at the leading edge. For lower radii, this simulation captures a transition near the trailing edge due to centrifugal instabilities for radii between $0.6R_b < r < 0.8R_b$, and LSB-induced transition near the blade's root, where the blade is thicker, inducing an adverse pressure gradient. With the increase of the Reynolds number, it is reasonable to think that the transition would advance to the mid chord and lies in the CD-segment in Figure **??**. However, the transition mechanism remains uncertain as LSB and centrifugal instabilities-induced transition could compete in this region.

In Figure **??**(b), at the pressure side, it becomes evident that accurately predicting the transition location is crucial. This figure highlights that the friction lines (dash-dotted black lines) deflect earlier than the actual onset of transition (dashed red lines). Additionally, it emphasizes the significance of the laminar cross-flow vortices in locally increasing the skin friction, as demonstrated in Figure **??**(c), compared to the location of turbulent transition as depicted in Figure **??**(b). These cross-flows occupy a substantial portion of the blade before undergoing destabilization through centrifugal instability mechanisms and transitioning into a fully turbulent state. Furthermore, centrifugal instabilities are observed in the transitional region close to the trailing edge around $0.70R_b \leq r \leq 0.75R_b$ (as shown in Figure **??**(a)). This region exhibits a turbulent transition, consistent with the predictions made in Figure **??** from (Carlton 2018).

3.5 Investigation of Centrifugal Instabilities

The analysis of the longitudinal streak breakdown in Figure **??** presents several features worth investigating. Vorticity contours, with isolines of radial velocity, are taken at different distances ξ from the leading edge. As the instability develops, the streaks are advected towards the blade tip (in the r direction on the horizontal axis) under the influence of centrifugal forces. Slices at $\xi = 0.70$ and $\xi = 0.75$ point out that the radial position influences the speed of the transitioning process. As the local Reynolds number increases through the blade's tip due to higher relative velocity, it leads to a faster transition to turbulence.

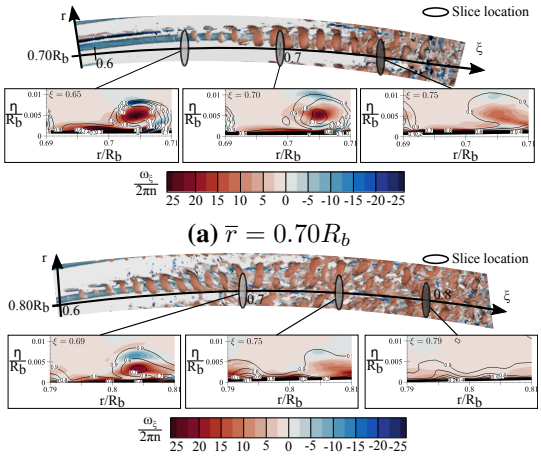

(a) $\overline{r} = 0.70R_b$

(b) $\overline{r} = 0.80R_b$

Figure 12: Evolution of the vorticity distribution in a longitudinal streak in the mean flow fields at the pressure side. λ_2-criterion snapshot are extracted from Figure ??(b)

The breakdown inception shows the centrifugal instability coherent structures developing, indicating the presence of a laminar flow. Figure **??** present slices of two centrifugal streaks located around $r = 0.7R_b$ and $0.8R_b$ respectively. Slicing across a longitudinal streak location allows us to see the vorticity evolution ω_z of the vortex as it moves downstream. The longitudinal streak does not form a symmetrical mushroom-like structure because of higher centrifugal forces. Its spatial evolution shows vortex roll-up as it moves away from the wall surface, illustrated experimentally in (Kohama 1984). At $r = 0.7R_b$, the vorticity of the lon-

gitudinal vortex decreases from $\omega_\xi = 50\pi n$ to $20\pi n$ as it destabilizes (see Figure **??**(a)). At $r = 0.8R_b$, Figure **??**(b) shows a more advanced transition of a longitudinal streak as it loses its coherence in slices. It also suggests that as the diameter of the laminar streak increases, the influence of the neighboring longitudinal streak can not be neglected as centrifugal forces shift the vortex in the spanwise direction.

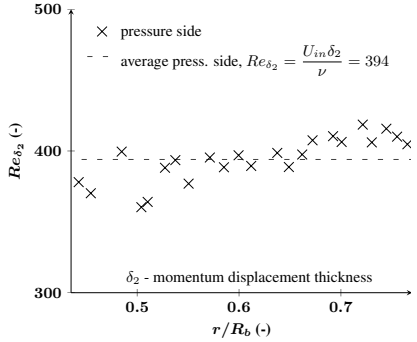

Figure 13: Evolution of the Reynolds number of the streak on the pressure side.

In the rotational disc case, Kohama (1984) characterized the streak inception using a constant critical Reynolds number for a given constant rotating velocity, highlighting the role of centrifugal instabilities. In this present simulation, the leading edge brings more complexity to the transition mechanisms. At the pressure side, without significant adverse pressure gradient, Figure **??** shows that streaks appear at a constant Reynolds number of about $Re_{\delta_2} = U_{in}\delta_2/\nu = 394$ along the blade's span.

4 CONCLUSION

This study investigated transitional boundary layer dynamics around a C-series marine propeller blade using U-DNS. The increase in Reynolds number from $220,000$ to $600,000$, with an advance coefficient of $J = 0.73$, points out the key role of centrifugal instabilities in the turbulent transition process on both sides of the blade.

The present work suggests that centrifugal instabilities could play a major role in the transition process of the boundary layer on marine propellers. The analysis of the transition mechanism led to a significant change in the transition point on most parts of the propeller blade. The deviation of friction lines, initially localized experimentally as the transition point, has been identified as the inception of longitudinal streaks. Hence, as centrifugal instabilities occur, the transition incepts more downstream and is onset by the breakdown of cross-flow vortices. This physic is particularly present at the pressure side, where the absence of adverse pressure gradient favors the development of these centrifugal instabilities. At the suction side, the simulation shows a more classical turbulent region from the critical radius up to the blade's tip. Below this region, the transition occurs more downstream, compared to the pressure side. It is due to an adverse pressure gradient, which stabilizes the boundary layer and delays centrifugal instabilities. Moreover, this paper suggests a possible competition of the centrifugal instability in the transition process with LSB-induced transition.

In the near future, the present method will be extended to other propeller geometries for various Reynolds numbers and advance coefficients to investigate further laminar to turbulent transition.

ACKNOWLEDGEMENT

This work was granted access to the HPC resources of IDRIS under the allocations 2021-[A0112A07686] and 2022-[A0132A07686].

REFERENCES

Baltazar, J. Melo, D. Rijpkema, D. (2020) 'Analysis of the Blade Boundary Layer Flow of a Marine Propeller Using a RANS Solver' Ocean Engineering, **211**, pp. 107633.

Carlton J. (2018) Marine Propellers and Propulsion. 4th ed. Butterworth-Heinemann

Choi, H. Moin, P. (2012), 'Grid-Point Requirements for Large Eddy Simulation: Chapman's Estimates Revisited'. Physics of Fluids, **24**(1), pp 011702.

Fischer, P. Kruse, J. Mullen, J. Tufo, H. Lottes, J. Kerkemeier, S. (2008). 'Nek5000: Open Source Spectral Element CFD Solver'. Argonne National Laboratory, Mathematics and Computer Science Division, Argonne, IL

Jessup, S.D. Scott, C.G. Jeffers, M.F., Kobayashi, S. (1985). Local Propeller Blade Flows in Uniform and Sheared Onset Flows using LDV (Laser Doppler Velocimetry) Techniques. David W. Taylor Naval Ship Research And Development Center.

Jing, Z. & Ducoin, A. (2020). 'Direct Numerical Simulation and Stability Analysis of the Transitional Boundary Layer on a Marine Propeller Blade'. Physics of Fluids **32**(12), pp. 124102.

Kohama, Y. (1984). 'Study on boundary layer transition of a rotating disk'. Acta Mechanica, **50**, pp 193-199.

Kuiper G. (1978). 'Scale Effect on Propeller Cavitation Inception'. Proceedings of the 12th ONRSymposium on Naval Hydrodynamic, Washington DC, USA.

Maday, Y. and Patera, A. (1989). 'Spectral element methods for the incompressible Navier-Stokes equations'. State-of-the-art surveys on computational mechanics, New York, USA.

Moran-Guerrero, A. Gonzalez-Gutierrez, L.M. Olivia-Remola, A. Diaz-Ojeda, H.R. (2018). 'On the Influence of Transition Modeling and Crossflow Effects on Open Water Propeller Simulation'. Ocean Engineering, **156**, pp 101-119.

NEK5000 Version 19.0. Release date : 28/12/2019. Argonne National Laboratory, Illinois.

Pawar, S. Brizzolara, S. (2019a). 'Relevance of Transition Turbulent Model for Hydrodynamic Characteristics of Low Reynolds Number Propeller'. Applied Ocean Research, **87**, pp 165.

Pawar, S. Brizzolara, S. (2019b). 'Hydroelastic Analysis of 3D Printed Marine Propeller Working at Low Reynolds Number'. Sixth International Symposium on Marine Propulsors, Rome, Italy.

Reed, H.L. Saric, W.S. (1989) 'Stability of Three-Dimensional Boundary Layers'. Annual Review of Fluid Mechanics, **21**(1), pp 235-284.

Shüelein, E. Rosemann, H. Schaber, S. (2012). 'Transition Detection and Skin Friction Measurements on Rotating Propeller Blades'. 28th Aerodynamic Measurement

Technology, Ground Testing and Flight Testing Conference.

Wilkinson, S. P. Malik, M.R. (1985). 'Stability experiments in the flow over a rotating disk'. AIAA Journal, **23**(4), pp 588–595.